Radiation damage in uranium dioxide: coupled effect between electronic and nuclear energy losses

Marion Bricout, Claire Onofri-Marroncle, Aurélien Debelle, Yves Pipon, Renaud Belin, Frederico Garrido, Frederic Lepretre, Gaelle Gutierrez

Radiation damage in uranium dioxide: coupled effect between electronic and nuclear energy losses

Marion Bricout[a], Claire Onofri[b], Aurélien Debelle[c,a], Yves Pipon[d], Renaud C. Belin[b], Frédérico Garrido[c], Frédéric Leprêtre[a], Gaëlle Gutierrez[a,]*

[a]CEA, DEN, Service de Recherche de Métallurgie Physique (SRMP), Laboratoire JANNUS, Université Paris-Saclay, F-91191, Gif-sur-Yvette, France

[b]CEA, DEN, Service d'Analyses d'Elaboration, d'Expérimentations et d'Examens des Combustibles (SA3E), Laboratoire LCPC, F-13108, Saint Paul-lez-Durance, France

[c]Centre de Sciences Nucléaires et de Sciences de La Matière (CSNSM), Université Paris-Sud, CNRS/IN2P3, Université Paris-Saclay, F-91405, Orsay campus, France

[d]Univ Lyon, UCBL, CNRS/IN2P3, IPNL – UMR 5822, F-69622 Lyon, France

Keywords: dual ion beam irradiation, uranium dioxide, Raman, TEM, XRD, dislocation loops

*Corresponding author: gaelle.gutierrez@cea.fr (G. Gutierrez)

Highlights:

- Induced mechanisms under dual-beam ion irradiation were studied in UO_2.
- Electronic ionizations lead to an accelerated defect rearrangement in UO_2.
- Fission fragments could generate partial recovery of the damage in nuclear fuel.

Abstract

A coupling between the nuclear and electronic energy losses occur in the nuclear fuel (UO_2) during in-reactor operations. However, the underlying mechanisms involved are still to be investigated. In this work, synergistic effects of nuclear and electronic energy losses have been investigated by irradiating crystals with single (900 keV I ions or 27 MeV Fe ions) and dual (900 keV I ions and 27 MeV Fe ions, simultaneously) ion beams at the JANNUS-Saclay facility. The damage build-up kinetic was *in situ* characterized by Raman spectroscopy. The microstructure evolution was determined by transmission electron microscopy (TEM) observations and by X-ray diffraction (XRD) analysis. Results show that both crystalline disorder and strain level are lower under dual-beam compared to the single-beam ion irradiations. Indeed, the dual-beam irradiation induces a transition from the formation of dislocation loops to dislocation lines. This result can be explained, in the framework of the thermal spike model, by a local increase of the temperature along the high-energy ion path. This temperature increase likely induces an enhanced defect migration leading to defect rearrangement.

1. Introduction

Uranium dioxide (UO_2) is the common fuel used worldwide in pressurized water reactors. Due to the fission chain reaction during the in-reactor operations, the UO_2 matrix is exposed to the simultaneous irradiation of neutrons, fission fragments, gamma, alpha and beta particles and alpha recoils. Fission fragments (FF) are the most damaging irradiation source. The FF have a kinetic energy ranging from 70 to 100 MeV. These high energy particles lose their energy via ionizations and electronic excitations in the fuel [1,2]. When the FF velocity decreases, these projectiles interact with matrix atoms by elastic collisions generating atomic displacements [3,4]. This particle-matter interaction induces a microstructure evolution with the formation of extended defects such as cavities, dislocation loops or lines in the UO_2 matrix. At a macroscopic scale, these evolutions can result in a swelling or a fuel restructuration.

In the past several decades, studies have been carried out to understand the fuel behaviour under irradiation. One way to investigate the involved mechanisms without dealing with highly radioactive matter is to perform ion beam irradiations of UO_2 depleted pellets. To identify the role played by either the nuclear or the electronic energy losses, the effect of each interaction has been separately investigated. Low-energy ion irradiation leads to point defect formation from the early stage of irradiation [5–7]. They rapidly grow into dislocation loops which evolve into dislocation lines after a few displacements per atom (dpa) for room-temperature irradiations [8–12]. Cavities are simultaneously formed and increase in size until a stabilized value of a few nanometres at about 0.3 dpa at room temperature [13–15]. These microstructural evolutions induce a significant modification of the strain level in the irradiated layer [16–18]. High-energy ion irradiation in UO_2, for electronic stopping power of 29 keV/nm, induces the formation of continuous ion tracks along the ion paths [19–22]. In the spent UO_2 fuel, tracks of fission products have never been observed. We can then supposed that the threshold value for the track formation occurs only for high electronic energy loss regime (between 22 and 29 keV/nm) [21]. However, to the best of our knowledge, no ion irradiation has been performed for stopping power range below 29 keV/nm.

Sequential irradiations of low-energy ions and high-energy ions were performed in UO_2 samples to determine the behaviour of implanted Xe ions under the effect of high-energy ions ionizations [23,24]. However, no information was reported regarding the microstructural evolution of the predamaged UO_2 lattice. Dual ion beam irradiations with low- (0.9 MeV I) and high-energy (36 MeV W) ions revealed a strain relaxation upon ionization induced by high energy ions as compared to low-energy irradiation. This result indicates that there is an ionization-induced change in the ballistic defect spectrum (both point and extended defects) [25]. It appears that a coupling between both stoppings - nuclear and electronic energy

losses - occurs in UO_2. However, the mechanisms behind this phenomenon remain unknown. In other materials, the effect of electronic excitations on the generated ballistic damages has shown different phenomena [26–33]. High-energy ion irradiation could either induce damage recovery as in SiC, MgO or borosilicates glasses [26–29] or enhance the damage production in the irradiated crystal as in $KTaO_3$ or c-ZrO_2 [30–32].

In the present work, our aim is to provide a better understanding of the interaction between nuclear and electronic energy losses in UO_2. For that purpose, single and dual-beam ion irradiations have been carried out, at room temperature (i.e. 298 K) in polycrystalline UO_2 discs with low- (0.9 MeV I) and high-energy (27 MeV Fe) ions separately, or simultaneously. The damage build-up was monitored by using the *in situ* Raman spectrometer [34]. Transmission electron microscopy (TEM) observations and x-ray diffraction (XRD) analysis were also performed on the UO_2 samples. The unified thermal spike (u-TS) model was applied to evaluate the temperature increase induced by electronic energy loss during high-energy ion irradiation [35].

2. Experimental details

Polycrystalline UO_2 pellets, with a mean grain size of 7.6 µm and a density equal to 97% of the theoretical one (i.e. 10.95 g.cm^{-3}), were cut into discs using a saw equipped with a diamond wire. Discs were further polished on one side down to a thickness of 500 µm and then annealed under an Ar-H_2 (5%) atmosphere at 1973 K for 24 h. They were mirror-polished with colloidal silica suspension and finally annealed under the same Ar-H_2 (5%) atmosphere at 1673 K for 4 h in order to maintain their stoichiometry (O/U = 2.00) [36].

UO_2 discs were irradiated at the JANNuS (Joint Accelerators for Nanoscience and Nuclear Simulation) Saclay facility [37]. Three experiments were performed: (1) single irradiation with 0.9 MeV I ion beam to a fluence of 8×10^{14} cm^{-2}; (2) single irradiation with a 27 MeV Fe ion beam to a fluence of 5×10^{14} cm^{-2}; (3) dual ion beam irradiation with 0.9 MeV I and 27 MeV Fe ion beams at the same fluences as in the single beam experiments. The low-energy I and high-energy Fe beams were delivered by the JAPET and EPIMETHEE accelerators, respectively, with ion fluxes limited to 10^{11} cm^{-2}s^{-1} in order to have a surface target heating smaller than 90 K during irradiation.

Irradiation parameters calculated using the SRIM code via the full cascade calculations mode are plotted in Fig.1 [38]. The threshold displacement energies for U and O were set to 40 and 20 eV, respectively [39,40]. As it can be seen in Fig.1, the electronic energy loss ($(dE/dx)_{elec}$) is predominant for 27 MeV Fe ions and the nuclear energy loss ($(dE/dx)_{nucl}$) is predominant for 0.9 MeV I ions over the thickness probed by the characterization techniques (i.e. ~1 µm). Thereafter the irradiation with the 27 MeV Fe ion beam will be referred to as S_e, the irradiation with the 0.9 MeV I one as S_n and the dual ion beam irradiation as S_n&S_e. In other words, S_n designates the ballistic regime and S_e the ionizing one.

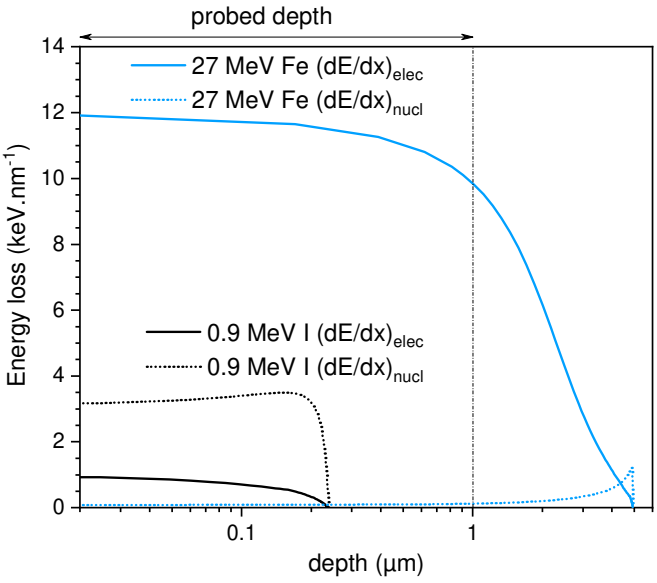

Fig. 1: Electronic and nuclear energy-loss depth distributions in UO_2 irradiated with 0.9 MeV I (referred as S_n) or 27 MeV Fe (referred to as S_e), as calculated with the SRIM software in full cascade mode. A density of 10.74 g.cm^{-3} was used and threshold displacement energies were set to 20 and 40 eV for the O and U sublattices, respectively [39,40]. *The electronic energy-loss is represented by straight lines, named $(dE/dx)_{elec}$ and the nuclear energy-loss by dotted lines, named $(dE/dx)_{nucl}$. The vertical dashed line at 1 µm represents the mean depth probed by XRD and Raman for the surface analysis.*

Irradiated samples were characterized using three complementary techniques: XRD, to measure the lattice parameter and evaluate the strain and stress levels, Raman spectroscopy, to follow the damage accumulation and TEM, to characterize extended defects.

XRD measurements were performed with a D8 Advance Bruker Diffractometer equipped with a copper source (Cu,$K_{\alpha1}$ and Cu,$K_{\alpha2}$). The XRD scans were recorded at a fixed incidence angle of 10° over a broad 2θ angular range (25°-110°). This incidence angle corresponds to an X-ray penetration depth of ~1.5 µm, considering an attenuation factor of 90 % [41].

Raman measurements were performed *in situ* during irradiation with the experimental setup described in [34]. Raman analyses were carried out using an Invia Reflex Renishaw spectrometer coupled with a Leica microscope with a frequency-doubled Nd:YAG (532 nm) laser and a 2400 groove / mm grating. A laser power less than 1 mW was used to avoid UO_2 oxidation. *In situ* Raman spectra were recorded for 120 s after beam shut-off at each step of irradiation fluence in the wave-number range from 180 and 850 cm^{-1}. In order to perform Raman measurements along the incident ion path, UO_2 cross-sections were prepared. The Raman spectrometer was calibrated with silicon single crystals. The effective laser penetration depth d, evaluated by $d = \frac{1}{2\alpha}$ with α the absorption coefficient, can be estimated to ~1 µm for our analysis conditions [42]. The fitting module of the WiRE Raman Spectroscopy software (Renishaw) was used for the spectra simulation with Voigt profiles. The accuracy on band position deduced from the spectrum simulation is estimated at ± 1 cm^{-1}.

The UO_2 irradiated samples were also observed by TEM. Electron-transparent thin foils were prepared by the Focused Ion Beam (FIB) technique at CP2M (Centre Pluridisciplinaire de Microscopie électronique et de Microanalyse) in Marseille, France. Cross-sections perpendicular to the implanted surface, protected by a platinum layer, were prepared to observe the microstructure after irradiation. The UO_2 thin foils were characterized with a FEI TALOS TEM operating at 200 kV at the LECA (Laboratoire d'Examens des Combustibles Actifs) in CEA Cadarache, France.

3. Results

The results are divided into two parts. First, a surface analysis (XRD and Raman spectroscopy) is presented to estimate the mean damage evolution over the probed depth (i.e. ~1 µm). Then, characterization of the samples cross-sections are displayed to evaluate the damage as a function of the probed depth by using TEM observations and Raman cartographies.

3.1 Surface analysis : evolution of the average disorder

3.1.1 XRD measurements

The $\sin^2\psi$ method was implemented following the procedure extensively described in [25] to determine the strain/stress state of the irradiated crystals. However, as we performed 2θ-scans, we implemented the multiple hkl reflection method so that the ψ angle varied with the Bragg angle of the probed reflections: $\psi = \theta_{\mathrm{Bragg}}^{\mathrm{hkl}} - \omega$ with ω the incident angle and θ_{Bragg}^{hkl} the Bragg angle [43]. As ω is fixed, an advantage of this method is that the penetration depth is kept constant.

Previous work showed a maximum average compressive in-plane stress of ~ -1 GPa (corresponding to an out-of-plane strain of about 0.6 %) for the 0.9 MeV I irradiated crystal. For the dual-beam irradiated crystal (0.9 MeV I and 36 MeV W, i.e. very similar to the present experiments), a lower stress level was observed (~-0.35 GPa), putting forward an effect of the dual-beam irradiation on the disorder build-up. A similar analysis was carried out for all the irradiated UO_2 polycrystals of the present study. A zoom of the 2θ-scans on the 331 and 420 reflections is displayed in Fig.2. The diffraction peaks of the crystal irradiated with S_n are split into two components [18,44]. On the high-angle side, two peaks (corresponding to $K_{\alpha1}$ and $K_{\alpha2}$ of the copper source) appear at the same 2θ value as for the unirradiated UO_2 crystal. They are associated with the unirradiated part of the crystal. Two additional peaks are observed at lower 2θ values, coming from the irradiated layer. After the dual-beam irradiation, only the two peaks from the irradiated layer are visible, because the unirradiated part is not probed. These two peaks are essentially due to the nuclear energy loss contribution of the high-energy Fe ions (as already suggested in [26] for instance). However, they exhibit tails that extend significantly and they are particularly asymmetric in the low-angle side. These features are likely related to the S_n effect, but clearly, the effect is different from that observed upon the single S_n irradiation. To more easily visualize this discrepancy, we plotted the peaks of the crystal irradiated with I ions along with those corresponding to the sample irradiated in the S_n&S_e regime, but we shifted these later so that they match those of the pristine material (see Fig. 2b). It is then more apparent that the asymmetry is related to the S_n effect, but the associated disorder must be drastically different to that created during

the S_n irradiation. This result provides another evidence that the S_n-generated defect spectrum has been modified upon the simultaneous ionization processes induced by S_e.

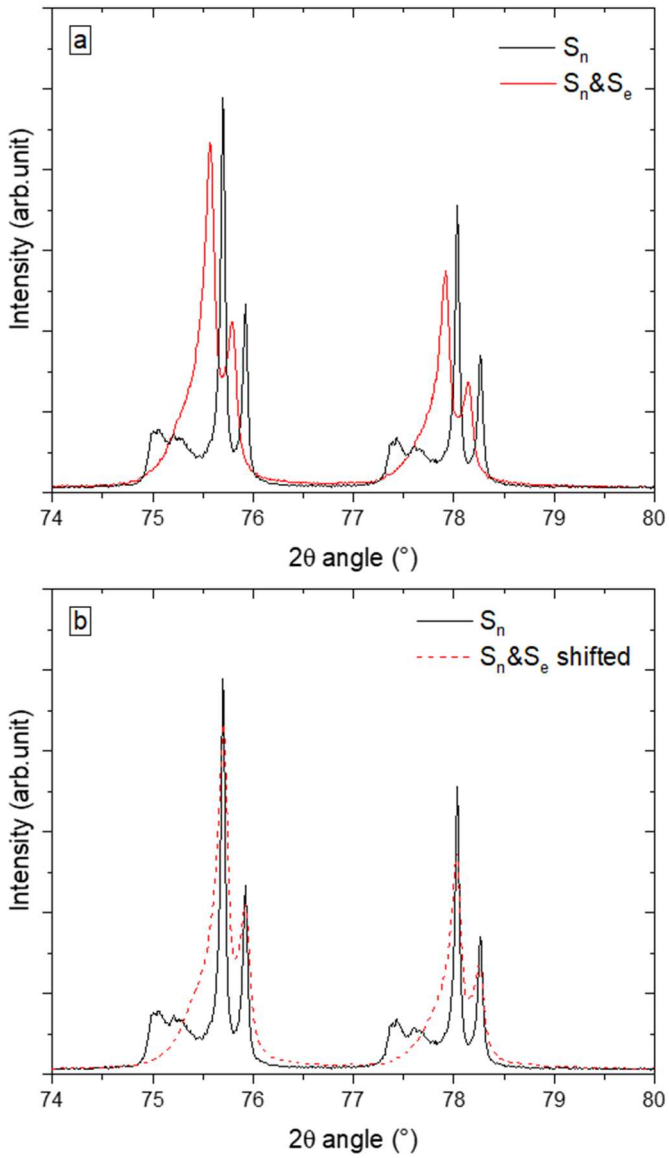

Fig. 2: (a) Two diffraction peaks, 331 and 420, taken from the full XRD pattern of irradiated UO_2 samples with S_n (black line) or with S_n&S_e (red line) recorded at a fixed incidence angle of 10°. (b) The same two peaks of the crystal irradiated with S_n&S_e, but shifted to match those of the pristine material.

Lattice parameters of the irradiated layers were determined by fitting all diffraction peaks (see Appendix, Fig.1) with pseudo-Voigt functions. They are plotted as a function of $\sin^2\psi$ in Fig. 3

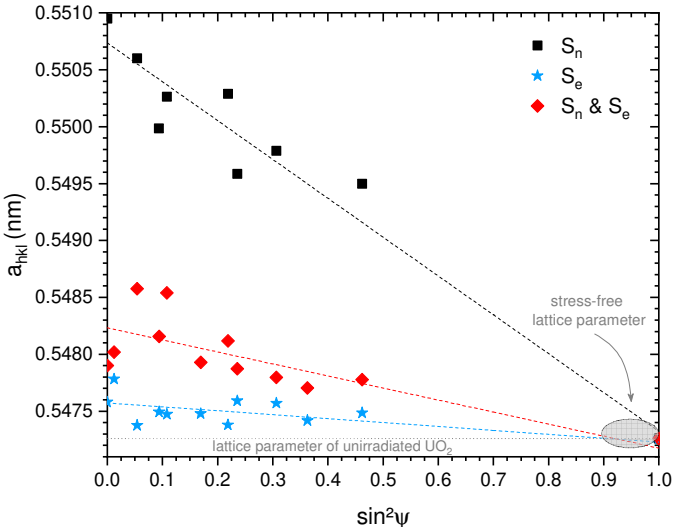

Fig. 3: Evolution of the lattice parameter, a_{hkl}, as a function of sin²ψ of irradiated UO_2: sample irradiated with S_n (black squares); sample irradiated with S_e (blue stars) and sample simultaneously irradiated with S_n&S_e (red diamond-shape symbols).

The negative slopes of the sin² ψ lines indicate a compressive in-plane stress experienced by the irradiated layers, as it was expected. All stress levels, along with strain levels (i.e. relative lattice parameter change) are reported in Table 1. The slope of the S_e-irradiated sample is very low. A very low-stress level is thus highlighted. This finding indicates that electronic excitations, at least in this energy-loss range, induce only a little disorder in UO_2. On the contrary, as expected, the stress estimated for the S_n-irradiated sample is high, ~ -1.1 GPa (in agreement with [25]). An intermediate stress is determined for the S_n&S_e irradiation, indicating that the stress generated by ballistic collisions has been either partially relaxed or its build-up has been prevented. This conclusion is in agreement with the previous statement of a change in the defect spectrum upon combined S_n&S_e irradiation.
In summary, it is shown that S_n&S_e irradiation induces a decrease of the measured strain and stress levels in comparison with S_n irradiation. Raman spectroscopy is then used to investigate the modification of the local disorder under S_n&S_e irradiation.

3.1.2 *In situ* damage build-up kinetics by Raman spectroscopy

Raman spectra were recorded *in situ* on the UO_2 samples during irradiation. As mentioned in [45], the spectrum of the unirradiated UO_2 exhibits the T_{2g} band at 445 cm^{-1}, corresponding to the triply degenerated Raman active mode, typical of the fluorite-type structure. The evolution of the T_{2g} bandwidth with the increase of the irradiation fluence is monitored step by step for the S_n irradiation in Fig.4(a). We observe a T_{2g} band broadening up to a value of 9 cm^{-1}, but no band shift occurs.

In addition to the T_{2g} band, the spectrum of the irradiated UO_2 exhibits three other bands in the 500-700 cm^{-1} range, namely U_1, LO, and U_3 (see Appendix, Fig.2). These three bands, associated with the local disorder in the UO_2 crystal, are referred to as the “triplet band” and are described elsewhere [45–48]. The LO band is a Raman-forbidden mode in the perfect fluorite-type structure becoming active with the presence of defects due to a breakdown in the selection rules. Because of a resonance effect in our analysis conditions, the LO band is much more intense as compared to the U_1 and U_3 bands. The LO band area has been normalized to avoid the discrepancies coming from the changes in the experiment conditions (laser focus and power, grain orientation distribution…). The evolution of the normalized LO band area is reported in Fig.4(b). After irradiation, an increase of the LO band area is observed from the first irradiation steps. It is followed by a stabilization occurring after a fluence of 5×10^{14} cm^{-2} (corresponding to about 1 dpa) as already report in [45] for similar value of damage level (few dpa) and even at higher damage level (up to 90 dpa for 4 MeV Kr ion irradiation).

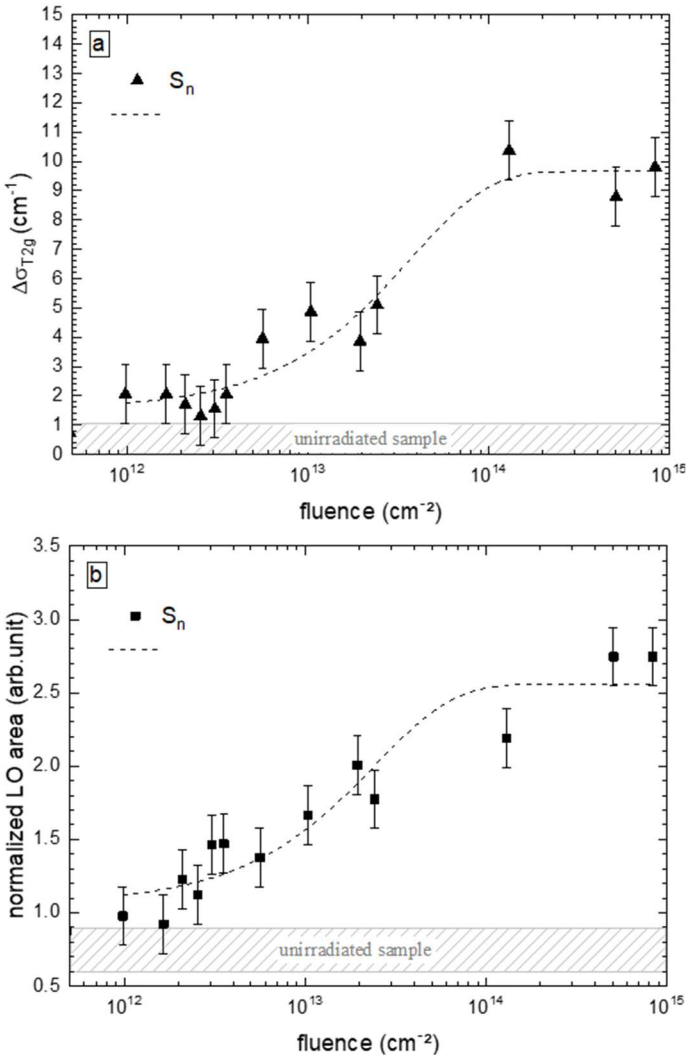

Fig. 4 : (a) Variation of the T_{2g} bandwidth and (b) the normalized LO band area for UO_2 irradiated samples with S_n up to 8×10^{14} cm^{-2}. The data are fitted with the MSDA model **[49]**.

A similar analysis has been performed for S_e and S_n&S_e irradiated samples. For an easier comparison of all the UO_2 samples, Fig. 5(a) presents the saturation level of the damage kinetics (i.e. the value at the signal saturation) for the various irradiations performed (S_e, S_n, and S_n&S_e). The S_e irradiation does not induce a large modification of the Raman spectrum neither for the T_{2g} band (broadening and position) nor for the LO band (area). Contrary to nuclear energy loss, electronic energy deposition induces little disorder in UO_2, but once again, as mentioned in the XRD section, at least in the electronic stopping amounts to 12 $keV.nm^{-1}$, far below the threshold for track formation. A T_{2g} band broadening is observed after the S_n&S_e irradiation (Fig.5(a)). In contrast, a large decrease of the LO band area of 39 ± 4 % is measured after the S_n&S_e irradiation as compared to the sole S_n irradiation.

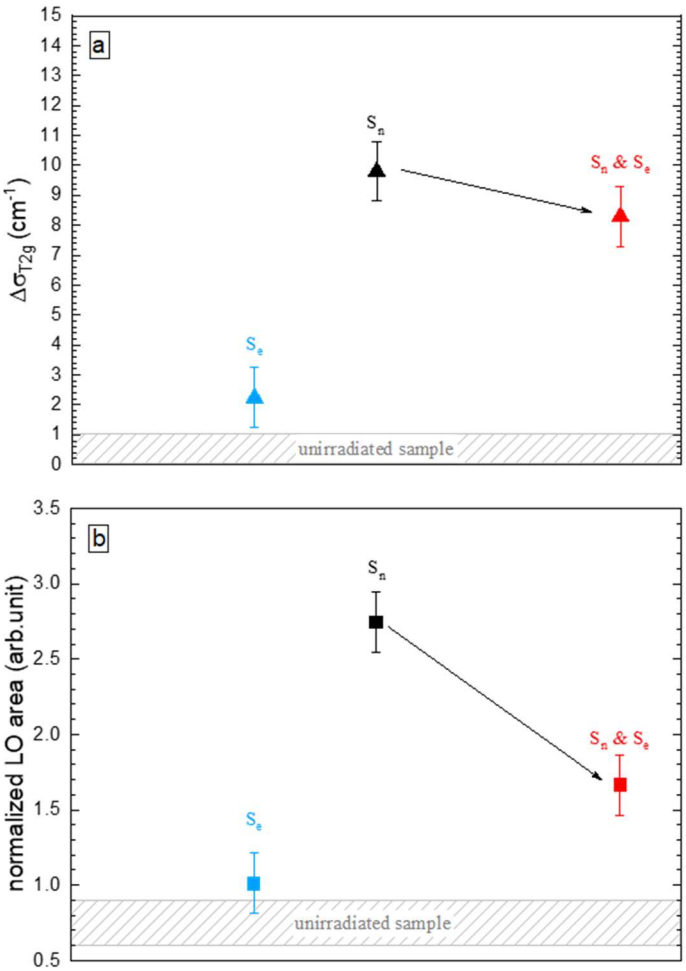

Fig. 5: Final (i.e. at the highest fluence of the damage build-up) (a) T_{2g} bandwidth and (b) normalized LO band area for a UO_2 sample irradiated in S_n and S_e regimes and for a UO_2 sample irradiated with the corresponding dual beam.

3.2 Cross-section analysis: depth distribution of damage

3.2.1 Raman line scans

In order to determine the depth profiles of the two disorder parameters obtained from Raman measurements, we performed a depth mapping of the S_n and S_n&S_e irradiated samples. From these maps, we extracted line scans every 0.2 µm and for each one, we determined the variation of the T_{2g} bandwidth (Fig.6(a)) and of the normalized LO band area (Fig.6(c)) as a function of the probed depth. The Raman spectra recorded at three different depths characteristic of the disorder profile (i.e. 0.7 µm, 5 µm and 7.5 µm) are shown in Fig.3 of the Appendix, for both S_n and S_n&S_e irradiated samples.

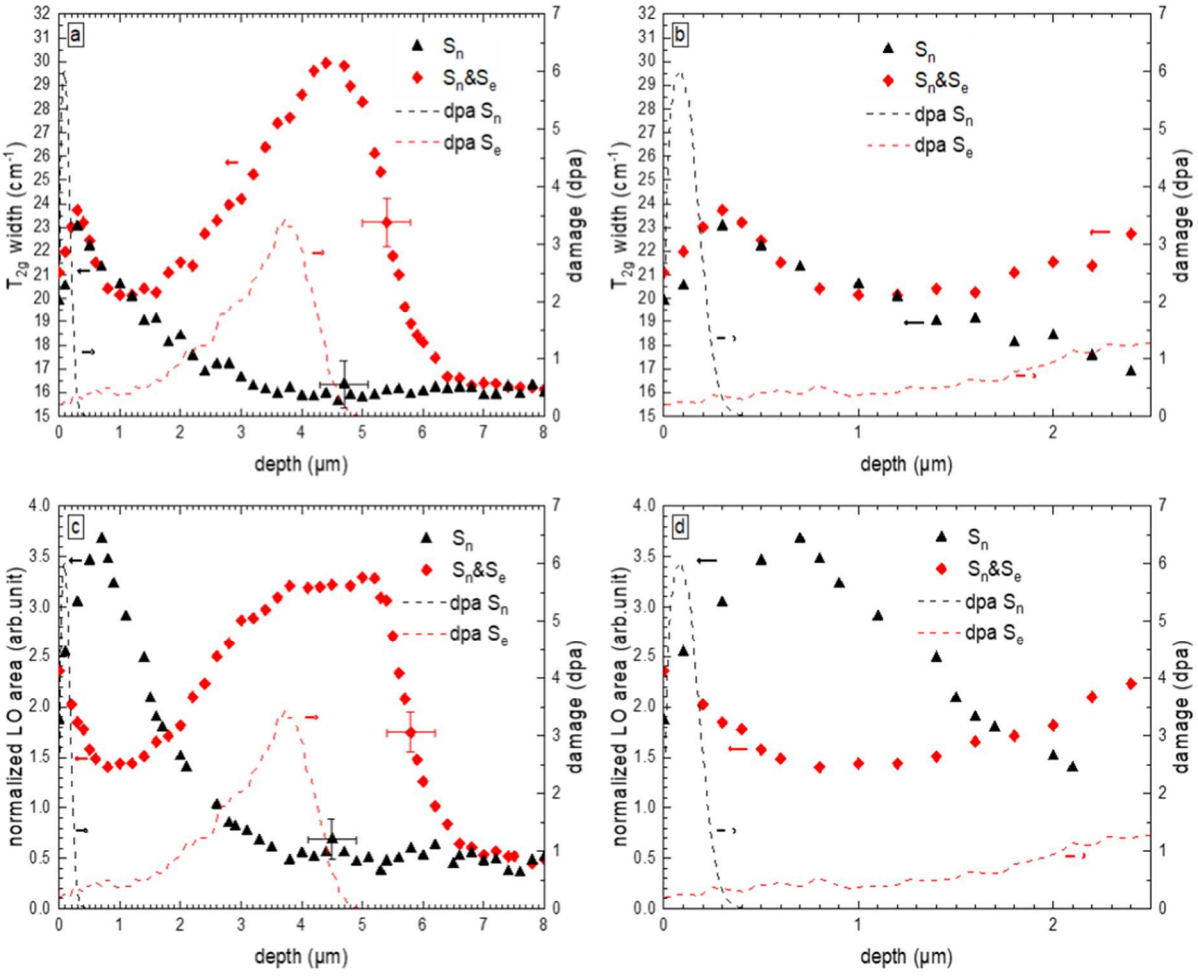

Fig. 6: Depth profiles of (a) the T_{2g} width and (b) the normalized LO band area of a UO_2 sample after the S_n irradiation (black triangles) and after the simultaneous S_n&S_e irradiation (red diamond-shape symbols). A zoom between 0 and 2.5 µm is displayed in (c) and (d). The right axis indicated the dpa level for the SRIM-calculated damage profiles in UO_2 upon S_n irradiation (black dash line) and upon S_e irradiation (red dash line). A depth of 0 µm corresponds to the sample surface. The X-axis error bars are associated with the laser spot

size, i.e. about 0.8 µm in our analysis conditions. To simplify the figure, only one X and Y error bars are represented.

After S_n irradiation, a maximum broadening of the T_{2g} band correlated with a maximum of the LO band area is observed at a depth range between 0.3 and 0.8 µm, in agreement with the maximum dpa calculated by SRIM for I ions at 900 keV (respectively, fig.6(b) and 6(d)). At greater depth, the two parameters decrease down to values similar to those of the unirradiated UO_2 samples, in accordance with the absence of radiation-induced damage in that area.

In the range between 0 and 0.3 µm that is affected by I ions, S_n&S_e irradiation has the same effect on the T_{2g} broadening as that induced by the sole S_n irradiation. However, the LO band area shows a strongly reduced intensity in comparison to the case of the sole S_n irradiation, revealing a modification in the local disorder.

We can note that, at a depth corresponding to the ballistic damage created by Fe ions (i.e. a depth higher than 2 µm), a broadening of the T_{2g} band coupled with an increase of the LO band area occur. However, the slight in depth discrepancy between the calculated dpa and the Raman signal may be assigned to the underestimation of the projected range of ions by the SRIM code and to the Raman depth resolution.

3.2.2 Microstructural evolution investigated by TEM

Fig.7 shows the cross-sectional TEM micrographs of the different irradiated samples. The arrows show the samples surface and the dotted lines represent the projected range of I ions.

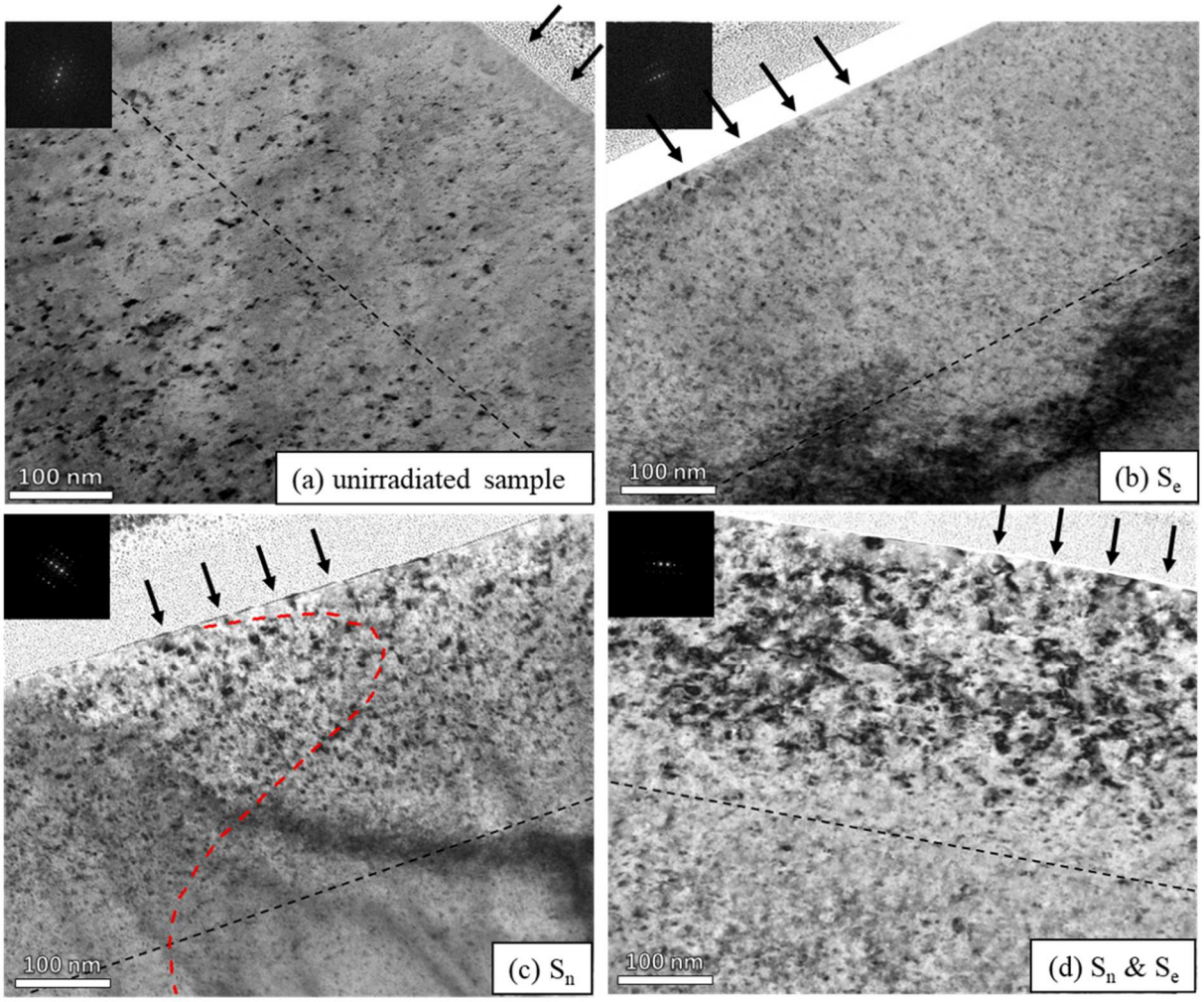

Fig. 7: Bright field TEM micrographs of (a) an unirradiated UO_2 sample, and samples irradiated (b) with Fe ions at a fluence of 5×10^{14} cm^{-2} (S_e), (c) with I ions at a fluence of 8×10^{14} cm^{-2} (S_n), and (d) simultaneously with I and Fe ions (S_n&S_e). Arrows and black dashed lines represent the implantation surface and the projected range of 0.9 MeV I ions, respectively. The red dashed curve in Fig.7(c) corresponds to the SRIM-predicted damage profile of I ions (S_n). The insets show the electron diffraction patterns. The diffraction vector is along <200>.

Fig. 7(a) presents the FIB lamella of an unirradiated sample. Dislocation loops are observed, indicating a significant defect formation induced by the preparation method. The micrograph of the S_e irradiated sample (Fig.7(b)) displays a higher defect density, but yet the disorder remains weak. This finding is consistent with the XRD and Raman results. In contrast, for S_n and S_n&S_e irradiations, we clearly observe significant changes in the image contrasts that reveal an important microstructural evolution. After the low-energy ion irradiation (S_n), a large density of dislocation loops are shown as black contrasts over a layer thickness of about 0.35 µm (Fig.7(c)), in good agreement with the ion projected range calculated by the SRIM code (Fig. 1 and red curve in Fig.7(c)). The sample subjected to the S_n&S_e irradiation (Fig.7(d)) still

exhibits some dislocation loops but it shows in addition many dislocation lines. We can notice that, at larger depth compared to I ions projected range, only FIB preparation defects are observed for both S_n and S_n&S_e irradiations.

4. Discussion

The S_n irradiation leads to an important microstructural modification. From the low fluence range, the disorder as probed by Raman spectroscopy increases. Indeed, it reveals the formation of point defects in the uranium sub-lattice as demonstrated by Mohun *et al.* [50]. The defect accumulation induces point defect clustering leading to the formation of extended defects, primarily dislocation loops as observed by TEM [8,25,45,51]. These microstructural changes induce a high strain measured by XRD, in agreement with previously reported results [16,18,25,44].

To explain the material modifications under dual beam irradiation, the inelastic thermal spike (iTS) model was applied in order to estimate the temperature increase in UO_2 after the passage of 27 MeV Fe ions for which the electronic stopping power is predominant. The iTS model was developed to estimate the ionization-induced temperature increase in insulators irradiated with Swift Heavy Ions (SHI) [52]. The atomic motion is assumed as a result of a transient thermal process [35,53]. Two steps are considered in the loss of the incident ions energy through the target material [54–56]. First, the incident ions transfer their energy to the electrons. This energy is transmitted to other electrons by electron-electron interactions. Then, the lattice is heated up by electron-phonon coupling. The electronic (e) and atomic (a) temperatures are governed by a set of coupled equations (eq. 1 and eq. 2) which describes the thermal energy deposited in a cylindrical slice of radius r as a function of time [21].

$$C_e(T_e)\frac{dT_e}{dt} = \frac{1}{r}\frac{d}{dr}\left[rK_e(T_e)\frac{dT_e}{dr}\right] - g(T_e - T_a) + A(r,t) \quad \text{Eq.1}$$

$$C_a(T_a)\frac{dT_a}{dt} = \frac{1}{r}\frac{d}{dr}\left[rK_a(T_a)\frac{dT_a}{dr}\right] + g(T_e - T_a) \quad \text{Eq.2}$$

Where *C* and *K* stand for the specific heats and thermal conductivities which are known for the UO_2 lattice [57]. A(r,t) corresponds to the distribution function of the incident ion energy deposition to the electronic sub-system [58]. As the hot electrons in the conduction band will behave like in metals, C_e and K_e are kept constant [21]. The parameter *g,* which is the electron-phonon coupling constant, is linked to the electronic mean free path (λ) chosen to be 4.5 nm [21]. The thermodynamic parameters of UO_2 used to calculate the deposited energy along the ion path are given in Table 2.

Table 2: Thermodynamical properties for UO_2.

Thermal properties	Value	Ref.
Thermal conductivity (W/K.cm)		
Solid (298 K)	0.076	[59]
Liquid (3121 K)	0.025	[60]
Specific heat *Cp* (J/g.K)		[61]
300	0.24	
700	0.30	
1000	0.31	

1500 **2000**	0.32 0.37	
Melting temperature (K)	3120	[62]
Vaporising temperature (K)	3815	[57]
Optical gap (eV)	2	[63]
Latent heat of fusion (J/g)	259	[57]
Latent heat of vaporisation (J/g)	1530	[57]
Mean specific mass (g/cm3) **Solid** **Liquid**	 10.63 8.86	 [64]

Calculations for 27 MeV Fe ion beam are displayed in Fig. 8 where the energy deposited on atoms is plotted for different distances from the projectile trajectory (radii).

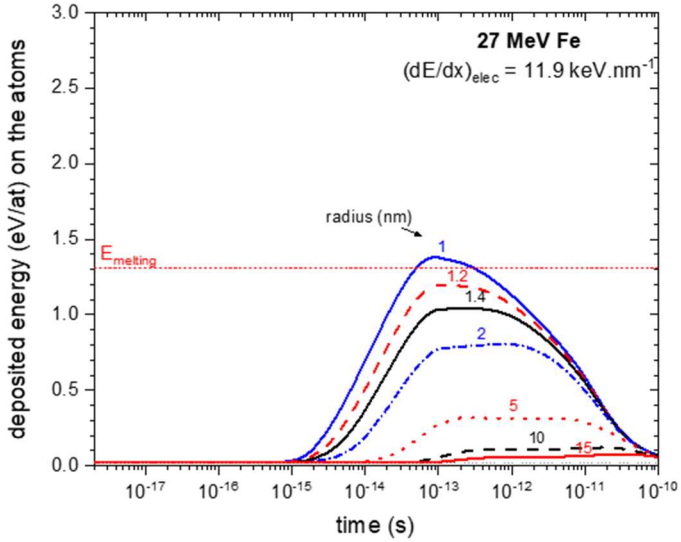

Fig. 8: Deposited energy as a function of time for 27 MeV Fe ions in a UO_2 target (S_e).

A maximum energy of ~1.4 eV is reached at about 10^{-13} s within a cylinder of radius of 1 nm. This energy surpasses the melting energy (1.31 eV.atom^{-1} [65]) but is far lower than the energy needed to reach the vaporization phase (2.68 eV.atom^{-1} [65]). Exceeding the vaporization energy is usually considered to be required to form tracks in these materials, which is not the case here. In contrast, this criterion might have been satisfied in [19–21,66] where the authors performed irradiations with a much larger S_e value. In our study, the calculated deposited energy on the atoms is not high enough to form observable latent tracks in UO_2. Only limited damage can be created because of the melting/quenching process in the vicinity of Fe ion path in the UO_2 matrix. This is correlated with the TEM observations for the S_e irradiation where no track has been revealed. In addition, we determine by XRD some weak, but measurable strain and, by Raman, the appearance of the triplet bands.

Whereas no significant damage creation is observed under S_e irradiation, the coupled effect of electronic excitations on the ballistic damages has been clearly highlighted under the S_n&S_e irradiation. The deposited energy by the S_e ion, calculated with the iTS model, is

sufficient to induce in a 10 nm radius the mobility of all the point defects. Indeed, both U and O lattice point defects in polycrystalline UO_2 become fully mobile at 973 K [2,67]. The local heating generated by the high-energy ions can lead to a recombination of point defects produced by low-energy ions and thus to a decrease of the local disorder. In addition, this defect migration during the S_n&S_e irradiation can induce a dislocation loop growth due to defect trapping at these dislocation loops. This growth leads to an early formation of dislocation lines compared to the S_n irradiation. Similar observations were made after irradiations at moderate temperature (from 773 K) where the transformation of dislocation loops into lines occurred at lower damage level [51,68]. However, the thermal spike occurs in a very short time (less than 1 ps) and may be less effective than an irradiation at high temperature due to the time factor limitation.

Thus, the local increase in temperature due to the electron-phonon coupling after the electronic energy deposition most likely leads to an accelerated defect rearrangement.

5. Conclusions

Ions beams irradiations were used to investigate the interaction between low- (S_n) and high-energy (S_e) ions. A clear effect of the electronic energy deposition on the generated ballistic damages was evidenced in UO_2 polycrystals simultaneously irradiated with a dual ion beam (S_n&S_e). XRD, Raman and TEM measurements presented in this work provide complementary information on the behaviour of the generated ballistic damages under electronic excitations. Although a decrease of the point defect density and a lower strain level are observed under dual beam irradiation, TEM observations indicate that electronic ionizations modify the defects generated by nuclear collisions. Indeed, an evolution from dislocation loops, generated by single S_n irradiation, to dislocation lines is highlighted for a similar S_n fluence under dual beam irradiation. By electron-phonon coupling, the lattice seems sufficiently heated up in the S_e ion path to induce a locally increased defect mobility. Dislocation loops may then act as traps for the smaller defects inducing their growth up to the formation of dislocation lines. All these results demonstrate that the electronic energy loss interact synergistically with the defects created by nuclear energy loss to modify the UO_2 matrix. This phenomenon depends on the irradiation parameters such as the irradiation temperature and the dose-rate of the high-energy ion beam. Future works will aim at characterizing the influence of these parameters on the microstructural evolution.

Acknowledgments

The technical staff of JANNuS-Saclay (Joint Accelerators for Nanoscience and Nuclear Simulation), CEA Paris-Saclay, France is greatly acknowledged for its support in performing irradiation experiments. Authors would like to thank J.-P. Crocombette, D. Gosset and M. Toulemonde, for fruitful scientific discussions.

References

[1] Whapham A. Electron Microscope Observation of Fission-Gas Bubble Distribution in UO2. Nucl Appl. 2 2 (1966) 123-.

[2] Whapham A, Sheldon B. Radiation damage in uranium dioxide. (1965) 1179.

[3] Martin G, Garcia P, Van Brutzel L, Dorado B, Maillard S. Effect of the cascade energy on defect production in uranium dioxide. Nucl Instrum Methods Phys Res Sect B-Beam Interact Mater At. 269 14 (2011) 1727–1730.

[4] Martin G, Garcia P, Sabathier C, Van Brutzel L, Dorado B, Garrido F, Maillard S. Irradiation-induced heterogeneous nucleation in uranium dioxide. Phys Lett A. 374 30 (2010) 3038–3041.

[5] Desgranges L, Simon P, Martin P, Guimbretiere G, Baldinozzi G. What Can We Learn From Raman Spectroscopy on Irradiation-Induced Defects in UO2? Jom. 66 12 (2014) 2546–2552.

[6] Desgranges L, Guimbretiere G, Simon P, Duval F, Canizares A, Omnee R, Jegou C, Caraballo R. Annealing of the defects observed by Raman spectroscopy in UO2 irradiated by 25 MeV He2+ ions. Nucl Instrum Methods Phys Res Sect B-Beam Interact Mater At. 327 (2014) 74–77.

[7] Mohun R, Desgranges L, Lechelle J, Simon P, Guimbretiere G, Canizares A, Duval F, Jegou C, Magnin M, Clavier N, Dacheux N, Valot C, Vauchy R. Charged defects during alpha-irradiation of actinide oxides as revealed by Raman and luminescence spectroscopy. Nucl Instrum Methods Phys Res Sect B-Beam Interact Mater At. 374 (2016) 67–70.

[8] Onofri C, Legros M, Lechelle J, Palancher H, Baumier C, Bachelet C, Sabathier C. Full characterization of dislocations in ion-irradiated polycrystalline UO2. J Nucl Mater. 494 (2017) 252–259.

[9] Ye B, Oaks A, Kirk M, Yun D, Chen W-Y, Holtzman B, Stubbins JF. Irradiation effects in UO2 and CeO2. J Nucl Mater. 441 1–3 (2013) 525–529.

[10] He LF, Pakarinen J, Kirk MA, Gan J, Nelson AT, Bai X-M, El-Azab A, Allen TR. Microstructure evolution in Xe-irradiated UO2 at room temperature. Nucl Instrum Methods Phys Res Sect B-Beam Interact Mater At. 330 (2014) 55–60.

[11] He L, Gupta M, A. Yablinsky C, Gan J, A. Kirk M, Bai X-M, Pakarinen J, Allen T. In situ TEM observation of dislocation evolution in Kr-irradiated UO2 single crystal. J Nucl Mater. 443 (2013) 71–77.

[12] Onofri C, Sabathier C, Baumier C, Bachelet C, Palancher H, Warot-Fonrose B, Legro M. Influence of exogenous xenon atoms on the evolution kinetics of extended defects in polycrystalline UO2 using in situ TEM. J Nucl Mater. 512 (2018) 297–306.

[13] Sabathier C, Martin G, Michel A, Carlot G, Maillard S, Bachelet C, Fortuna F, Kaitasov O, Olivier E, Garcia P. In-situ TEM observation of nano-void formation in UO2 under irradiation. Nucl Instrum Methods Phys Res Sect B-Beam Interact Mater At. 326 (2014) 247–250.

[14] Michel A, Sabathier C, Carlot G, Kaitasov O, Bouffard S, Garcia P, Valot C. An in situ TEM study of the evolution of Xe bubble populations in UO2. Nucl Instrum Methods Phys Res Sect B-Beam Interact Mater At. 272 (2012) 218–221.

[15] He LF, Valderrama B, Hassan A-R, Yu J, Gupta M, Pakarinen J, Henderson HB, Gan J, Kirk MA, Nelson AT, Manuel MV, El-Azab A, Allen TR. Bubble formation and Kr distribution in Kr-irradiated UO2. J Nucl Mater. 456 (2015) 125–132.

[16] Debelle A, Crocombette J-P, Boulle A, Chartier A, Jourdan T, Pellegrino S, Bachiller-Perea D, Carpentier D, Channagiri J, Nguyen T-H, Garrido F, Thome L. Lattice strain in irradiated materials unveils a prevalent defect evolution mechanism. Phys Rev Mater. 2 1 (2018) 013604.

[17] Debelle A, Boulle A, Garrido F, Thome L. Strain and stress build-up in He-implanted UO2 single crystals: an X-ray diffraction study. J Mater Sci. 46 13 (2011) 4683–4689.

[18] Nguyen T-H, Debelle A, Boulle A, Garrido F, Thome L, Demange E. Mechanical response of UO2 single crystals submitted to low-energy ion irradiation. J Nucl Mater. 467 (2015) 505–511.

[19] Ishikawa N, Sonoda T, Sawabe T, Sugai H, Sataka M. Electronic stopping power dependence of ion-track size in UO2 irradiated with heavy ions in the energy range of similar to 1 MeV/u. Nucl Instrum Methods Phys Res Sect B-Beam Interact Mater At. 314 (2013) 180–184.

[20] Garrido F, Choffel C, Dran J-C, Thome L, Nowicki L, Turos A. Structural modifications in uranium dioxide irradiated with swift heavy ions. Nucl Instrum Methods Phys Res Sect B Beam Interact Mater At. 127–128 (1997) 634–638.

[21] Wiss T, Matzke Hj, Trautmann C, Toulemonde M, Klaumünzer S. Radiation damage in UO2 by swift heavy ions. Nucl Instrum Methods Phys Res Sect B Beam Interact Mater At. 122 3 (1997) 583–588.

[22] Pisarev VV, Starikov SV. Atomistic simulation of ion track formation in UO2. J Phys-Condens Matter. 26 47 (2014) 475401.

[23] Marchand B, Moncoffre N, Pipon Y, Bererd N, Garnier C, Raimbault L, Sainsot P, Epicier T, Delafoy C, Fraczkiewicz M, Gaillard C, Toulhoat N, Perrat-Mabilon A, Peaucelle C. Xenon migration in UO2 under irradiation studied by SIMS profilometry. J Nucl Mater. 440 1–3 (2013) 562–567.

[24] Djourelov N, Marchand B, Marinov H, Moncoffre N, Pipon Y, Bererd N, Nedelec P, Raimbault L, Epicier T. Study of temperature and radiation induced microstructural changes in Xe-implanted UO2 by TEM, STEM, SIMS and positron spectroscopy. J Nucl Mater. 443 1–3 (2013) 562–569.

[25] Gutierrez G, Gosset D, Bricout M, Onofri C, Debelle A. Effect of coupled electronic and nuclear energy deposition on strain and stress levels in UO2. J Nucl Mater. 519 (2019) 52–56.

[26] Thome L, Velisa G, Miro S, Debelle A, Garrido F, Sattonnay G, Mylonas S, Trocellier P, Serruys Y. Recovery effects due to the interaction between nuclear and electronic energy losses in SiC irradiated with a dual-ion beam. J Appl Phys. 117 10 (2015) 105901.

[27] Zhang Y, Sachan R, Pakarinen OH, Chisholm MF, Liu P, Xue H, Weber WJ. Ionization-induced annealing of pre-existing defects in silicon carbide. Nat Commun. 6 (2015) 8049.

[28] Debelle A, Backman M, Thome L, Weber WJ, Toulemonde M, Mylonas S, Boulle A, Pakarinen OH, Juslin N, Djurabekova F, Nordlund K, Garrido F, Chaussende D. Combined experimental and computational study of the recrystallization process induced by electronic interactions of swift heavy ions with silicon carbide crystals. Phys Rev B. 86 10 (2012) 100102.

[29] Mir AH, Peuget S, Toulemonde M, Bulot P, Jegou C, Miro S, Bouffard S. Defect recovery and damage reduction in borosilicate glasses under double ion beam irradiation. Epl. 112 3 (2015) 36002.

[30] Jin K, Zhang Y, Weber WJ. Synergistic effects of nuclear and electronic energy deposition on damage production in KTaO3. Mater Res Lett. 6 9 (2018) 531–536.

[31] Thome L, Velisa G, Debelle A, Miro S, Garrido F, Trocellier P, Serruys Y. Behavior of nuclear materials irradiated with a dual ion beam. Nucl Instrum Methods Phys Res Sect B-Beam Interact Mater At. 326 (2014) 219–222.

[32] Zhang Y, Wang X, Liu S, Tang M, Zhao Z. Characterisation of dual ion beam irradiated yttria-stabilised zirconia by specific analytical techniques. Nucl Instrum Methods Phys Res Sect B Beam Interact Mater At. C 342 (2015) 52–61.

[33] Toulemonde M, Assmann W, Zhang Y, Backman M, Weber WJ, Dufour C, Wang ZG. Material transformation: Interaction between nuclear and electronic energy losses. In: Angeli F, Delaye JM, Schuller S, Pinet O, Rebiscoul D, Gin S, Peuget S, editors. 2nd International Summer School on Nuclear Glass Wasteform: Structure, Properties and Long-Term Behavior (sumglass 2013). Amsterdam: Elsevier Science Bv; 2014. p. 272–277.

[34] Miro S, Bordas E, Thomé L, Costantini J-M, Leprêtre F, Trocellier P, Serruys Y, Beck L, Gosset D, Verlet R, Huguet-Garcia J, Tupin M, Belleil M. Monitoring of the microstructure of ion-irradiated nuclear ceramics by in situ Raman spectroscopy. J Raman Spectrosc. 47 4 (2016) 476–485.

[35] Dufour C. Models for the Description of Track Formation. In: Toulemonde M, Wesch W, Wendler E, editors. Ion Beam Modification of Solids: Ion-Solid Interaction and Radiation Damage [Internet]. Springer International Publishing; 2016 [cited 2019]. p. 63–104. (Springer Series in Surface Sciences; vol. 61). Available from: https://www.springer.com/de/book/9783319335599

[36] Matzke Hj, Turos A. Erratum: Surface damage in UO2 due to mechanical polishing and ion bombardment. J Nucl Mater. 114 2 (1983) 349–352.

[37] Gentils A, Cabet C. Investigating radiation damage in nuclear energy materials using JANNuS multiple ion beams. Nucl Instrum Methods Phys Res Sect B Beam Interact Mater At. 447 (2019) 107–112.

[38] Ziegler JF, Ziegler MD, Biersack JP. SRIM - The stopping and range of ions in matter (2010). Nucl Instrum Methods Phys Res Sect B-Beam Interact Mater At. 268 11–12 (2010) 1818–1823.

[39] Soullard J. High-Voltage Electron-Microscope Observations of UO2. J Nucl Mater. 135 2–3 (1985) 190–196.

[40] Meis C, Chartier A. Calculation of the threshold displacement energies in UO2 using ionic potentials. J Nucl Mater. 341 1 (2005) 25–30.

[41] Simeone D, Baldinozzi G, Gosset D, Le Caer S, Berar J-F. Grazing incidence X-ray diffraction for the study of polycrystalline layers. Thin Solid Films. 530 (2013) 9–13.

[42] Griffiths TR, Hubbard HVStA. Absorption spectrum of single-crystal UO2: Identification of and effect of temperature on the peak positions of essentially all optical transitions in the visible to near infrared regions using derivative spectroscopy. J Nucl Mater. 185 3 (1991) 243–259.

[43] Welzel U, Ligot J, Lamparter P, Vermeulen AC, Mittemeijer EJ. Stress analysis of polycrystalline thin films and surface regions by X-ray diffraction. J Appl Crystallogr. 38 1 (2005) 1–29.

[44] Richard A, Castelier E, Palancher H, Micha JS, Rouquette H, Ambard A, Garcia P, Goudeau P. Multi-scale X-ray diffraction study of strains induced by He implantation in UO2 polycrystals. Nucl Instrum Methods Phys Res Sect B-Beam Interact Mater At. 326 (2014) 251–255.

[45] Gutierrez G, Onofri C, Miro S, Bricout M, Lepretre F. Effect of ballistic damage in UO2 samples under ion beam irradiations studied by in situ Raman spectroscopy. Nucl Instrum Methods Phys Res Sect B-Beam Interact Mater At. 434 (2018) 45–50.

[46] He H, Shoesmith D. Raman spectroscopic studies of defect structures and phase transition in hyper-stoichiometric UO2+x. Phys Chem Chem Phys. 12 28 (2010) 8109–8118.

[47] Livneh T. Coupling of multi-LO phonons to crystal-field excitations in UO(2) studied by Raman spectroscopy. J Phys-Condens Matter. 20 8 (2008) 085202.

[48] Desgranges L, Guimbretiere G, Simon P, Jegou C, Caraballo R. A possible new mechanism for defect formation in irradiated UO2. Nucl Instrum Methods Phys Res Sect B-Beam Interact Mater At. 315 (2013) 169–172.

[49] Jagielski J, Thome L. Multi-step damage accumulation in irradiated crystals. Appl Phys - Mater Sci Process. 97 1 (2009) 147–155.

[50] Mohun R, Desgranges L, Jegou C, Boizot B, Cavani O, Canizares A, Duval F, He C, Desgardin P, Barthe M-F, Simon P. Quantification of irradiation-induced defects in UO2 using Raman and positron annihilation spectroscopies. Acta Mater. 164 (2019) 512–519.

[51] Onofri C, Sabathier C, Baumier C, Bachelet C, Palancher H, Legros M. Evolution of extended defects in polycrystalline Au-irradiated UO2 using in situ TEM: Temperature and fluence effects. J Nucl Mater. 482 (2016) 105–113.

[52] Toulemonde M. Thermal spike model in the electronic stopping power regime. Radiat Eff Defects Solids. 126 205 (1993) .

[53] Sigmund P, Claussen C. Sputtering from elastic-collision spikes in heavy-ion-bombarded metals. J Appl Phys. 52 2 (1981) 990–993.

[54] Toulemonde M, Dufour C, Meftah A, Paumier E. Transient thermal processes in heavy ion irradiation of crystalline inorganic insulators. Nucl Instrum Methods Phys Res Sect B-Beam Interact Mater At. 166 (2000) 903–912.

[55] Toulemonde M, Weber WJ, Li G, Shutthanandan V, Kluth P, Yang T, Wang Y, Zhang Y. Synergy of nuclear and electronic energy losses in ion-irradiation processes: The case of vitreous silicon dioxide. Phys Rev B. 83 5 (2011) 054106.

[56] Meftah A, Costantini JM, Khalfaoui N, Boudjadar S, Stoquert JP, Studer F, Toulemonde M. Experimental determination of track cross-section in Gd3Ga5O12 and comparison to the inelastic thermal spike model applied to several materials. Nucl Instrum Methods Phys Res Sect B-Beam Interact Mater At. 237 3–4 (2005) 563–574.

[57] Mathew PM, Jiang Y, Mares R, Froment K, Sengupta AK, Hwang IS, Kim YS, Fortov V, Efanov A, Fink JK, Jaroma-Weiland G. Thermophysical properties database of materials for light water reactors and heavy water reactors. International Atomic Energy Agency (IAEA); 2006 Jun. Report No.: IAEA-TECDOC-1496.

[58] Mieskes HD, Assmann W, Gruner F, Kucal H, Wang ZG, Toulemonde M. Electronic and nuclear thermal spike effects in sputtering of metals with energetic heavy ions. Phys Rev B. 67 15 (2003) 155414.

[59] Belle J. Uranium Dioxyde: Properties and Nuclear Applications. Washington, D.C.: Government Printing Office; 1961.

[60] Ronchi C. On the thermal conductivity and diffusivity of solid and liquid uranium dioxide. J Phys Condens Matter. 6 38 (1994) L561–L567.

[61] Fink JK, Chasanov MG, Leibowitz L. Thermophysical properties of uranium dioxide. J Nucl Mater. 102 1 (1981) 17–25.

[62] Matzke Hj. Radiation damage in nuclear materials. Nucl Instrum Methods Phys Res Sect B Beam Interact Mater At. 65 1 (1992) 30–39.

[63] Freeman AJ, Lander GH. North-Holland, Amsterdam; 1984. 185 p. (Handbook on the Physics and Chemistry of the Actinides; vol. I).

[64] Belle J, Berman RM. Thorium dioxide: properties and nuclear applications [Internet]. USDOE Assistant Secretary for Nuclear Energy; 1984 [cited 2019]. Report No.: DOE/NE--0060. Available from: http://inis.iaea.org/Search/search.aspx?orig_q=RN:16071971

[65] Toulemonde M, Benyagoub A, Trautmann C, Khalfaoui N, Boccanfuso M, Dufour C, Gourbilleau F, Grob JJ, Stoquert JP, Costantini JM, Haas F, Jacquet E, Voss K-O, Meftah A. Dense and nanometric electronic excitations induced by swift heavy ions in an ionic CaF2 crystal: Evidence for two thresholds of damage creation. Phys Rev B. 85 5 (2012) 054112.

[66] Hayashi K, Kikuchi H, Fukuda K. Radiation damage of UO2 by high-energy heavy ions. J Nucl Mater. 248 (1997) 191–195.

[67] Nakae N, Iwata Y, Kirihara T. Thermal Recovery of Defects in Neutron-Irradiated Uo2. J Nucl Mater. 80 2 (1979) 314–322.

[68] Debelle A, Crocombette J-P, Boulle A, Martinez E, Uberuaga BP, Bachiller-Perea D, Haddad Y, Garrido F, Thomé L, Béhar M. How relative defect migration energies drive

contrasting temperature-dependent microstructural evolution in irradiated ceramics. Phys Rev Mater. 2 8 (2018) 083605.

[69] Gaillac R, Pullumbi P, Coudert F-X. ELATE: An open-source online application for analysis and visualization of elastic tensors. J Phys Condens Matter. 28 (2016) .

List of Tables

List of Figures